Improved Electrical Performance of Perovskite Photovoltaic Mini-Modules through Controlled PbI$_2$ Formation Using Nanosecond Laser Pulses for P3 Patterning

Markus Fenske, Christof Schultz,* Janardan Dagar, Felix Utama Kosasih, Andreas Zeiser, Cornelia Junghans, Andreas Bartelt, Caterina Ducati, Rutger Schlatmann, Eva Unger, and Bert Stegemann

The upscaling of perovskite solar cells to modules requires the patterning of the layer stack in individual cells that are monolithically interconnected in series. This interconnection scheme is composed of three lines, P1–P3, which are scribed using a pulsed laser beam. The P3 scribe is intended to isolate the back contact layer of neighboring cells, but is often affected by undesired effects such as back contact delamination, flaking, and poor electrical isolation. Herein, the influence of the laser pulse duration on the electrical and compositional properties of P3 scribe lines is investigated. The results show that both nanosecond and picosecond laser pulses are suitable for P3 patterning, with the nanosecond pulses leading to a higher open circuit voltage, a higher fill factor, and a higher power conversion efficiency. It is found that the longer pulse duration resultes in a larger amount of PbI$_2$ formed within the P3 line and a thin Br-rich interfacial layer which both effectively passivate defects at the scribe line edges and block charge carrier in its vicinity. Thus, nanosecond laser pulses are preferable for P3 patterning as they promote the formation of beneficial chemical phases, resulting in an improved photovoltaic performance.

1. Introduction

Metal halide perovskites (MHPs) are very promising light-absorber materials for low-cost and highly efficient solar modules. They are characterized by a long charge-carrier lifetime ($\approx$100 ns), a strong optical absorption ($\approx 10^5$ cm^{-1}), and a moderate carrier mobility ($\approx$100 cm^2 Vs^{-1}), making it well suited for optoelectronic applications.[1] Moreover, the broad tunability of their bandgap makes this material class a strong contender for tandem cell applications.[2–4] As high power conversion efficiencies (PCE) have been achieved for lab-scale perovskite solar cells (PSCs),[5] the next step toward commercialization is to scale up these tiny cells into perovskite solar modules (PSMs) of industrially relevant sizes. For this purpose, a reliable patterning process to create the cell-to-cell monolithic series interconnection needs to be developed. This interconnection scheme is obtained by alternating layer deposition and patterning steps referred to as P1, P2, and P3. The P1 and P3 patterning steps are used to electrically separate the front and back contact layer of neighboring cells, respectively, whereas the P2 patterning step provides an electrical path between the back contact of one cell and the front contact of the adjacent cell by locally removing the absorber and charge transport layers. A pulsed laser is the tool of choice for PSM patterning as it enables layer-selective material ablation and high reproducibility due to its noncontact nature. The general principles of laser patterning of thin films are described in our earlier work.[6] These principles and approaches have been widely applied to the full laser patterning of PSMs,[7–10] with most attention given to

---

M. Fenske, Dr. C. Schultz, Prof. A. Zeiser, Prof. A. Bartelt,
Prof. R. Schlatmann, Prof. B. Stegemann
School of Engineering – Energy and Information
HTW Berlin – University of Applied Sciences
Wilhelminenhofstr. 75a, Berlin D-12459, Germany
E-mail: schultz@htw-berlin.de

Dr. J. Dagar, Dr. E. Unger
Young Investigator Group Hybrid Materials Formation and Scaling
Helmholtz-Zentrum Berlin für Materialien und Energie
Kekuléstraße 5, Berlin D-12489, Germany

F. U. Kosasih, Prof. C. Ducati
Department of Materials Science & Metallurgy
University of Cambridge
27 Charles Babbage Road, Cambridge CB3 0FS, UK

Dr. C. Junghans
Becker & Hickl GmbH
Nunsdorfer Ring 7-9, Berlin D-12277, Germany

Prof. R. Schlatmann
Photovoltaics Competence Centre Berlin (PVcomB)/Helmholtz-Zentrum Berlin für Materialien und Energie
Schwarzschildstr.3, Berlin D-12489, Germany

the P2 step for patterning of the perovskite absorber layers. Nevertheless, several challenges regarding the P3 patterning step have been reported. In 2015, Moon et al.[11] showed fully laser-patterned PSMs but reported flaking of the back contact layer and difficulties in achieving good electrical isolation between neighboring cells. There, proper electrical isolation was achieved using ns laser pulses and wider P3 lines with overlapping rows of patterning, but flaking of the back contact still occurred. In 2019, Kosasih et al.[12] investigated the P3 patterning step using ps laser pulses. They observed two different morphologies of back contact delamination, depending on the degree of overlap between adjacent laser pulses and the resulting effective laser fluence (cf. Haas et al.[13]). In addition, compositional alterations in the perovskite layer next to the scribe line edge were observed, which can be seen in the decomposition of perovskite into needle-shaped PbI_2 grains.[12] The influence of PbI_2 on the overall photovoltaic performance of a PSC is still under controversial discussion in the community. Recent reports have identified several drawbacks due to the presence of excess PbI_2. These include parasitic absorption losses,[14] poorer charge-carrier transport,[15] lower photostability,[16] and accelerated device degradation.[17] However, other reports indicate that excess PbI_2 could have beneficial effects such as passivation of electronic defects at voids, grain boundaries and defects,[16,18] increased shunt resistance,[19] and improved charge extraction.[15]

Moreover, there are partly contradictory observations on the role of PbI_2 even in recent work, making it impossible to draw general conclusions at present.[15,20] Therefore, further investigations are needed to exploit the advantages and disadvantages of PbI_2. We aim to contribute to this discussion with our work by deliberately controlling the laser-induced formation of PbI_2 to improve the photovoltaic performance of PSMs. As the requirements for high-quality P2 and P3 lines are contrary (i.e., P2: low contact resistance, P3: high isolation resistance), we expect that material modifications during the last patterning step such as the laser-induced decomposition of the perovskite to PbI_2 have a completely different role in optimizing the electrical functionality of the P3 contact and may be even beneficial.

Our approach is to analyze the laser-scribed P3 lines and their vicinity with regard to its electrical behavior and material composition. As challenges for P3 patterning have been reported for both ns and ps laser pulses, in this study we used both a ns laser and a ps laser operating at the same wavelength of 532 nm. Longer pulse durations deposit more thermal energy into the target material, which can propagate away from the original target area through the material lattice.[6,7] These ns/ps P3 lines were scribed on 3-cell PSMs with an active area of 2.2 cm^2 per module. The parameters for P1 and P2 patterning are the same for all samples (see Section 2.2). The electrical functionality of the PSMs was evaluated by current density–voltage (j–V) measurements to derive a window of suitable laser fluences for P3 patterning. The morphology and chemical composition of the prepared P3 lines and its surrounding area were then analyzed using scanning electron microscopy (SEM) and energy-dispersive X-ray spectroscopy in a scanning transmission electron microscope (STEM-EDX). Spectrally filtered photoluminescence (PL) measurements were used to map the spatial distribution of PbI_2 within the scribe lines. In addition to the experimentally determined scribe line properties, an approximation of the laser-induced surface temperature is given using a simple model based on the 1D heat equation.

2. Experimental Section

2.1. Sample Preparation

The preparation of the PSMs follows the procedure for (n-i-p) perovskite baseline samples reported in refs. [8,21]. There, standard glass substrates with an area of 2.5×2.5 cm^2 were coated with 120 nm-thick indium tin oxide (ITO; $R_{sq} \approx 15\ \Omega\ cm^{-2}$). Subsequently, the ITO front contact layer was P1 patterned. Afterward, the samples were cleaned in an ultrasonic bath, first in a soap solution, deionized water, acetone and then in isopropanol for 15 min each. After drying with N_2, the substrates were UV–ozone treated for 15 min. The SnO_2 solution was prepared by dissolving $SnCl_2\cdot2H_2O$ in ethanol and overnight stirring at room temperature. In the next step, the SnO_2 electron transport layer (ETL) was deposited by spin-coating; first at a speed of 1500 rpm for 30 s and then ramped to a speed of 2500 rpm for another 30 s. The ETL was cured at 180 °C in ambient atmosphere, its final thickness was about 23 nm.[21] The triple cation perovskite solution $Cs_{0.05}FA_{0.79}MA_{0.16}PbBr_{0.51}I_{2.49}$ was spin-coated following the standard procedure described in previous studies[21,22]; the thickness of the perovskite layer was typically in the range of 550 nm. For the preparation of hole transport layer (HTL), a 36.2 mg mL^{-1} concentration of spiro-OMeTAD precursor was dissolved in chlorobenzene and then finally doped with 4-*tert*-butylpyridine (TBP) (14.4 µL mL^{-1}), Li-bis (trifluoro-methanesulfonyl)imide (Li-TFSI) (8.8 µL mL^{-1}), and cobalt (III) complex (14.5 µL mL^{-1}) dopants. The spiro-OMeTAD solution was spin-coated over the perovskite film at a spin speed of 1800 rpm for 30 s, resulting in a final thickness of about 190 nm.[23] After that, the sample was P2 patterned. Finally, a 100 nm gold back contact was evaporated under low pressure as the back contact layer and subsequently P3 patterned to complete the monolithic series interconnection of the PSMs. For this study, about 120 PSMs were fabricated. In **Table 1**, a list of all materials used for sample fabrication is given; after their purchase from the supplier, the materials were directly used for device fabrication without further modification.

2.2. Laser Patterning

The patterning of the PSMs was carried out using a commercial laser system (Rofin Baasel Lasertech). It was equipped with a ns laser source (SL3PV) emitting laser pulses with a wavelength of 532 nm and a pulse duration of about 20 ns. The maximum pulse energy of 32 µJ was achieved at 20 kHz, resulting in a maximum fluence of 10.3 J cm^{-2} for a beam diameter of 28.1 µm $\pm$ 10% in focal position. In addition, a ps laser source (Time Bandwidth, Duetto) was installed, emitting laser pulses of a wavelength of 1064 and 532 nm with a pulse duration of about 10 ps. The pulse repetition rate (PRR) for P3 patterning was 100 kHz, corresponding to a maximum pulse energy of about 25 µJ, resulting in a maximum fluence of 8.7 J cm^{-2} for a beam diameter of 26.7 µm $\pm$ 10% in focal position when the wavelength was set at 532 nm. The laser beam diameters were determined by

Table 1. Materials and solutions used for PSM fabrication.

Materials	Supplier
Formamidinium iodide (FAI)	Dynamo
Methylammonium bromide (MABr)	Dynamo
4-tert-butylpyridine (TBP)	Dynamo
Cobalt (III) complex	Dynamo
Indium tin oxide covered glass substrates	Lumtec
Spirobifluorene (spiro-OMeTAD) ($\geq$99.8%)	Merck
Tin chloride (SnCl22H2O) dehydrate	Sigma-Aldrich
DMSO (Dimethyl sulfoxide anhydrous, $\geq$99.9%)	Sigma-Aldrich
DMF (N,N-Dimethylformamide anhydrous, 99.8%)	Sigma-Aldrich
Chlorobenzene	Sigma-Aldrich
Ethanol (99.8%)	Sigma-Aldrich
Cesium iodide (CsI)	Sigma-Aldrich
Li-bis (trifluoromethanesulfonyl)imide (Li-TFSI)	Sigma-Aldrich
Tin chloride dihydrate (SnCl$_2$•2H$_2$O)	Sigma-Aldrich
Lead (II) iodide (99.99%, trace metals basis)	TCI Deutschland GmbH
Lead bromide (PbBr$_2$)	TCI Deutschland GmbH

applying the method of Liu.[24] The sample translation for patterning was realized using an x–y motion system, enabling velocities up to 1.2 m s^{-1} while the positioning accuracy was well below 5 µm for each stage; the laser beam was guided via fixed optics to the sample surface. To avoid material degradation and to collect debris, the samples were patterned in a patterning chamber with a continuous nitrogen flow. The P1 patterning process was performed using the ps laser operating at a wavelength of 1064 nm. To achieve a clean and even surface of the P1 trench, a high pulse-to-pulse overlap ($\approx$93%) was applied. These P1 scribe lines achieved a high electrical isolation of neighboring cells (>20 MΩ). For P2 patterning, the ps laser operating at a wavelength 532 nm was applied. The P2 scribe line was multiple (3×) patterned without a lateral displacement to achieve a clean and smooth scribe line surface, enabling low contact resistance for series interconnection[8]; the pulse-to-pulse overlap was about 63%. The P3 scribe lines were multiple patterned (3×) without any lateral displacement to maintain a narrow interconnection width and to achieve good electrical separation of neighboring cells. Thereby, the laser fluence for both ns and ps pulses was systematically varied, so that a wide range from slight surface

modifications to the ablation of the whole stack including the onset of ITO damage could be investigated and a suitable window of patterning parameters could be determined. The pulse-to-pulse overlap was about 12% for a single pass. By scribing the line three times, homogeneous material removal and constant scribe line widths were achieved. To enable a transfer of the achieved results to different substrate materials (i.e., flexible substrates), the patterning steps were carried out from the layer side (direct ablation). The fabricated PSMs had an active area of 2.22 cm^2 (3 × 0.74 cm^2) and an aperture ratio of slightly above 90%, based on a cell width of 5 mm and a dead area width of about 0.5 mm. All patterning parameters are summarized in **Table 2**.

2.3. Characterization Techniques

The surface morphology of the P3 lines and their surrounding areas were imaged using SEM operated in secondary electron mode. Specifically, Figure 3a,b were acquired using a Hitachi S4100 SEM operated at 5 kV, while Figure 3c,d were acquired using a FEI Nova NanoSEM operated at 2 kV. The cross-sectional lamellae for STEM-EDX were prepared with a FEI Helios Nanolab Dualbeam FIB/SEM according to a standard procedure.[25] The lamellae were immediately transferred into a FEI Osiris (S)TEM operated at 200 kV with air exposure minimized to $\approx$2 min. High-angle annular dark-field (HAADF) images were acquired with a Fischione detector with a dwell time of 1 µs/pixel. The STEM-EDX spectrum images were obtained with a Bruker Super-X silicon drift detector with a solid collection angle of about 0.9 sr. To minimize beam damage, a defocused beam ($\Delta f = -1$ µm) with a beam current of about 130 pA, a dwell time of 30 ms/pixel, and spatial sampling of 10 nm/pixel was used.[26] The STEM-EDX data was denoised with principal component analysis and processed in HyperSpy, a Python-based analysis suite for hyperspectral data.[27] Spectrally filtered PL microscopy measurements were performed using a commercially available fluorescence lifetime imaging (FLIM) setup (Becker & Hickl, DCS 120) equipped with a 488 nm pulsed ps diode laser (BDS-SM, Becker & Hickl) and a photosensitive detector module (B&H, HPM-100). The electrical functionality of the PSMs was probed using an AAA-class solar simulator (Wavelabs Sinus 70), operated with an irradiance of 1000 W m^{-2} and a calibrated light spectrum corresponding to an air mass of 1.5. The solar simulator was calibrated using a silicon reference cell (Fraunhofer ISE). To avoid any possible effect of sample heating,

Table 2. Process parameters used for laser patterning.

	Unit	P1	P2	P3 ns	P3 ps
Wavelength [λ]	nm	1064	532	532	532
Pulse duration [τ_P]	s	$\approx 10^{-11}$	$\approx 10^{-11}$	$\approx 2^{-8}$	$\approx 10^{-11}$
Beam diameter [$2\omega_0$]	µm	21.5 ($\pm$10%)	26.7 ($\pm$10%)	28.1 ($\pm$10%)	26.7 ($\pm$10%)
Scribing velocity [v]	mm s^{-1}	400	200	500	500
Pulse repetition rate [PRR]	kHz	250	20	20	20
Pulse overlap	%	$\approx$93	$\approx$63	$\approx$11	$\approx$7
Laser fluence [F]	J cm^{-2}	7.3	1.16	1.36	2.31

the PSMs were placed on a temperature-controlled sample holder during the j–V measurement. Each PSM was measured in forward and reverse directions with a resolution of 0.05 V/step at an integration time of 20 ms and a delay time of 40 ms.

2.4. Calculation of the Laser-Induced Surface Temperature

Calculation of the laser-induced surface temperature was carried out using a model that was developed to calculate the laser-induced heat flow as described in detail in our previous work.[8] There, the calculation was based on the theoretical work of Bulgakova et al.[28–31] and Meshcheryakov and Bulgakova[32] who have worked out the fundamentals of laser-material interaction. This model has been adapted for the specific task of approximating the laser-induced surface temperature in a direction perpendicular to the laser scribe line. The model corresponds to a 50 µm-long, thermally insulated bar made of Au. By including an additional term, the latent heats of fusion and vaporization were considered; whereas, losses due to convection as well as the spatial heat flow were neglected. The boundary conditions were set as follows: for the sample surface $dT/dz = 0$ (no convectional losses) and the remote boundary temperature was set to a fixed value of 300 K. This preliminary calculation approximates the temperature distribution in the Au contact layer perpendicular to the laser scribe line. **Table 3** summarizes all material properties used for the calculation of the surface temperature.

3. Results and Discussion

3.1. Electrical Characterization

The investigation of the influence of the laser fluence on the electrical parameters aims to establish suitable laser fluence ranges, both for ns and ps patterning, that enable the fabrication of devices with high average performance that are robust and tolerant to preparation-related sample-to-sample variations of the material properties. The electrical parameters of the laser-patterned PSMs are used as an indicator to assess a range of suitable laser fluences for P3 patterning. From the measured j–V curves, the fill factor (FF) and PCE were derived. FF and PCE are useful metrics for evaluating the quality of P3 lines as they are sensitive to series and shunt resistances, two parameters that can be strongly affected by P3 line quality. The series resistance may become too

high if the ITO layer is damaged during P3 scribing, whereas the shunt resistance may become too low if the back contact removal is insufficient or if flaking or delamination occurs, as this leads to electrical short circuits. **Figure 1** shows the derived PCEs of the PSMs as a function of the laser fluence used for P3 patterning by ps (Figure 1a) and ns (Figure 1b) laser pulses. Despite the relatively broad spread of values, clear trends can be observed for both ns and ps laser pulses. As indicated in the graph, in the case of patterning with ps laser pulses, the highest average and top PCEs (above 17%) can be achieved at a fluence of 2.31 J cm^{-2}. At a lower fluence of 1.08 J cm^{-2}, the average efficiency is similarly good, but the top efficiencies are lower. This indicates a wide range of suitable fluences for successful P3 patterning. However, to achieve the highest PCE and also to ensure that a complete separation of the absorber layer has been achieved, a fluence of 2.31 J cm^{-2} was selected for the preparation of the PSMs. In the case of patterning with ns laser pulses, a similar distribution of PCEs is seen at fluences of 1.04 and 1.36 J cm^{-2} with top PCEs of above 19%. This also indicates a wide range of suitable fluences and, thus, a rather tolerant process here. The higher fluence of 1.36 J cm^{-2}, however, is preferred for further patterning, because less back contact flakes and remaining material splashes and debris were observed next to the trenches (cf. Figure S1, Supporting Information). Such features do not necessarily lead

Table 3. Material properties used for numerical analysis of laser-induced surface temperature.

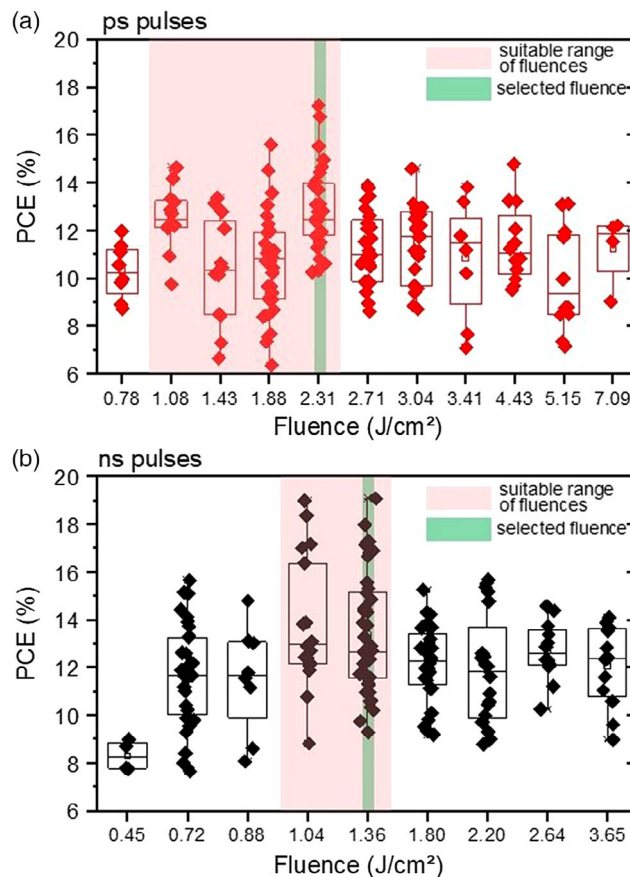| Properties	Unit	Gold[39,40]
Absorption coefficient [α] @ 532 nm	cm^{-1}	5.27 E + 05
Heat capacity [c_p]	J kg^{-1} K^{-1}	129.1
Thermal conductivity [κ]	W mK^{-1}	320
Mass density [ρ]	g cm^{-3}	19.3
Melting point [T_b]	K	1337
Boiling point [T_b]	K	3128
Latent heat of fusion	kJ g^{-1}	0.063
Latent heat of vaporization	kJ g^{-1}	1.67

Figure 1. Box-plot of the mini-module PCE as a function of the applied laser fluence for P3 patterning by a) ps and b) ns laser pulses.

to a loss of performance, but should be avoided due to the enhanced risk of shunts.

Fluences below and above the suitable ranges might lead to lower PCEs for both ps and ns pulses. This behavior is to be expected as too low fluences would result in incomplete material removal and poor electrical isolation of neighboring cells, whereas excessively high fluences have a high probability of damaging the front contact layer underneath due to the thermal impact.[8,12] From this point on, all discussion about ns- and ps-scribed P3 lines refers to those patterned with the selected fluences, as shown in Figure 1.

Figure 2 shows the $j–V$ curves of two typical 3-cell PSMs, in which the series interconnection was achieved by P3 patterning with ns (black curve) or ps (red curve) laser pulses. In both cases, P2 patterning was done by ps laser pulses. The results show that both ns and ps laser pulses are suitable for P3 patterning, with the ns pulses leading to a slightly higher open-circuit voltages (V_{oc}) and higher FF resulting in a higher overall PCE. The $j–V$ curves for single cells as well as for two-segmented mini-modules were added to the graph to demonstrate the successful series interconnection and the multiplication of the V_{oc} of the single cell. An overview on the solar cell parameters is given in **Table 4**. Moreover, the statistical evaluation of the measurements on all PSMs is provided in the Supporting Information (see Figure S2, Supporting Information). The given values of series (R_{oc}) and shunt resistances (R_{sc}) were derived from the slope of the $j–V$ curves at the V_{oc} and short-circuit current (J_{sc}) points under illumination, respectively. Accordingly, PSMs with ns-scribed P3 lines exhibit lower series (see Table 4) and higher shunt resistances (see Figure S2b, Supporting Information), resulting in higher V_{oc}, higher FF, and higher PCE. The origin of these differences will now be examined in the following sections through a comprehensive analysis of the material properties in the trench and its vicinity.
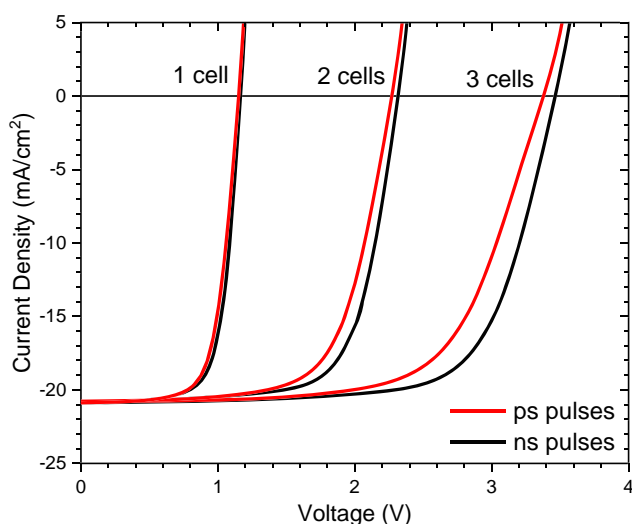
Table 4. Measured $j–V$ characteristics of the PSM shown in Figure 2, patterned by ps and ns laser pulses with fluences of 2.31 and 1.36 J cm^{-2}, respectively.

	Single cell	2 interconnected cells	3 interconnected cells
P3 ns laser patterning			
Power conversion efficiency [%]	17.30	17.07	16.97
Fill factor [%]	71.12	70.97	70.49
V_{oc} [V]	1.17	2.31	3.46
R_{sc} [Ω cm^2]	9.419	19.972	28.108
R_{oc} [Ω cm^2]	0.008	0.035	0.079
P3 ps laser patterning			
Power conversion efficiency [%]	16.69	15.87	15.40
Fill factor [%]	69.47	67.41	65.80
V_{oc} [V]	1.15	2.27	3.38
R_{sc} [Ω cm^2]	6.688	14.608	27.590
R_{oc} [Ω cm^2]	0.008	0.040	0.108

3.2. Morphological and Compositional Analysis

To ensure proper electrical isolation between adjacent cells and to minimize the dead area width, back contact delamination and flaking as well as the occurrence of residues must be limited. The surface morphology of P3 lines and its surrounding area was thus investigated by SEM imaging. **Figure 3**a,b show that both ns- and ps-scribed P3 lines have constant widths and sharp edges with minimal delamination and no flaking. The ITO layer inside the lines is also visible, with some residual material appearing as grains and debris on the trench surface. These grains are shown in Figure 3c,d at higher magnification. The most interesting difference between the trench surfaces is the number of needle-shaped grains located there. Only a few of them appear in the ps-scribed P3 line (Figure 3c), whereas there is a high number of these needles in the ns-scribed P3 line (Figure 3d). These needle-shaped grains have previously been assigned to PbI$_2$, in good agreement with its crystal structure.[18,33] PbI$_2$ is known to be a common product of thermal decomposition of perovskite[34]; so from Figure 3c,d, we can infer that the ns pulses deposit a sufficiently large amount of thermal energy to trigger compositional changes beyond the volume of the ablated material. This energy deposition and its subsequent propagation indicate the possibility of changes in the perovskite composition in the active area of the module, as previously shown.[8,9] We prepared cross-sectional lamellae for STEM imaging and STEM-EDX analysis to investigate whether and how the perovskite structure is modified by the P3 scribing process. **Figure 4** shows cross-sectional HAADF images and STEM-EDX elemental maps of three lamellae: one reference lamella cut far from any scribe line and one each from next to an ns- or ps-scribed P3 line. For the latter two lamellae, the left edge of the images and maps are closest to the P3 line edge. The images and maps of the reference and ps-scribed lamellae look largely similar. In both samples,
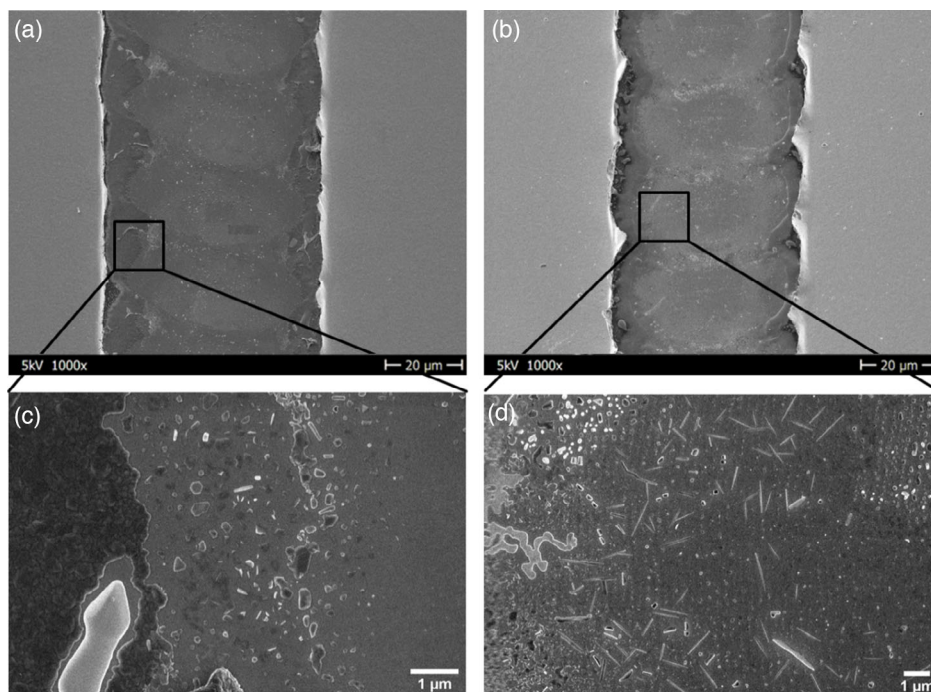

Figure 2. $j–V$ curves of 3-segmented mini-modules, patterned with fluences of 2.31 and 1.36 J cm^{-2} by ns laser pulses (black) and ps laser pulses (red), respectively. The curves both for single cells and for 2-segmented mini-modules are also shown. P2 patterning was done by ps laser pulses.

Figure 3. SEM images of the laser-scribed lines patterned by a) ps and b) ns laser pulses with fluences of 2.31 and 1.36 J cm^{-2}, respectively. The black squares schematically show the positions of the high-magnification images of the c) ps and d) ns laser scribe lines.
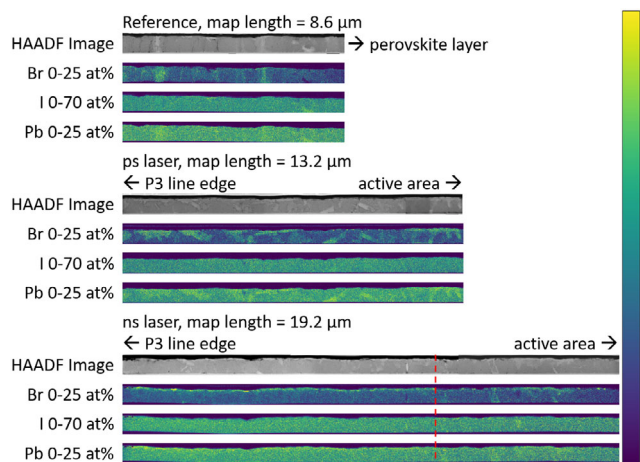

Figure 4. Cross-sectional HAADF images and STEM-EDX elemental maps (Br, I, and Pb) of the reference, ps-scribed, and ns-scribed lamellae. The left end of these images and maps is located next to the P3 line edge, whereas the right end is furthest into the active area. The red dashed line mark the end of the Br-rich layer formed in the ns-scribed sample, 12 μm from the P3 line edge.

the perovskite layer contains grains which are Br- and (slightly) Pb-rich while the iodine distribution is homogeneous throughout. Only the number of these grains differ, with more of them appearing in the ps sample than in the reference. On the other hand, the elemental maps of the ns sample reveal the presence of a thin Br-rich (and I-poor) layer at the perovskite/HTL interface. This layer extends for about 12 μm into the active area, as marked by the red dashed line in Figure 4. The Br-rich grains found in the reference and the ps-scribed sample do not exist within this distance, but reappear again beyond the 12 μm mark. Although these are preliminary results, these maps suggest a remixing of bromine and lead close to the edge of ns-scribed P3 lines, which appears to convert the morphology of the Br- and Pb-rich area from distinctively shaped grains to a thin layer. Previously, the presence of such a Br-rich layer at the perovskite/HTL interface has been shown to improve charge-carrier collection by acting as a hole-blocking layer, a role made possible by its wider bandgap compared with the stoichiometry of the thermally unaffected perovskite.[35] The STEM analysis suggests that the thermal impact of the ns laser pulse promotes the local decomposition of perovskite in the vicinity of the laser-scribed lines. This is likely to cause the formation of PbI$_2$ inside the P3 line (cf. Figure 3) and a Br-rich layer in the adjacent active area. Both, PbI$_2$ and Br-rich perovskite are larger bandgap semiconductors that should effectively passivate defects at the scribe line edges and block charge carriers in its vicinity.[18,35] In comparison, we observe that only a few PbI$_2$ grains are present in the ps-scribed P3 line, with minimal compositional changes in the nearby active area compared with the reference.

3.3. Analysis of the PL Images

Spectrally filtered PL spectroscopy was applied to confirm the presence of PbI$_2$ within the P3 lines. Therefore, the PL emission was spectrally filtered using a band-pass filter with a width of 40 nm, transmitting light only of wavelengths between 490 and 530 nm, thus corresponding to the optical bandgap of
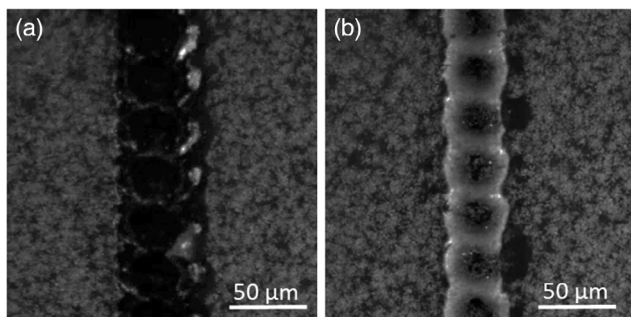
Figure 5. Comparison of spectrally filtered PL intensity images of P3 laser scribe lines patterned with a) ps and b) ns laser pulses at fluence. A (510 ± 20) nm band-pass filter was used that transmits the characteristic emission of PbI_2.

Figure 6. Calculated spatial decay of the temperature, induced by a ns laser pulse with a fluence of 1.36 J cm^{-2}. The y-axis is scaled logarithmically. The vertical dotted line marks the distance from the scribe line edge where the lamella for cross-sectional STEM-EDX was cut. This is also indicated by the black rectangle at the lower end of the graph. The area with a Br-rich layer is marked.

PbI_2 at room temperature ($\approx$520 nm; cf. Figure S3, Supporting Information).[36,37] In **Figure 5**, the corresponding PL intensity images of a) ps- and b) ns-scribed P3 lines are shown. Evidently, only a low emission is detected within the ps-scribed P3 line, which corresponds to low amounts of PbI_2. In contrast, the ns-scribed P3 line in Figure 5b shows regions of bright PL, which are centered around the assumed positions of individual laser shots during the patterning step. In both cases, a homogeneous PbI_2 signal was observed over the whole sample surface, which is due to the excess ($\approx$9%) of PbI_2 in the triple cation stoichiometric during preparation. The PL data show that ns laser processing resulted in far more PbI_2 residues inside the P3 lines compared with ps laser processing. This corroborates the interpretation of needle-like features observed in the P3 trench by SEM imaging (Figure 3d) to stem from PbI_2.

3.4. Numerical Analysis of the Laser-Induced Heat-Flow

As explained in Section 1, ns laser pulses deposit more thermal energy in the target material than ps laser pulses. It is therefore likely, that thermal effects are responsible for the formation of PbI_2 and the Br-rich layer in the ns-scribed PSMs as described earlier. To support this hypothesis, we used a 1D heat decay model (see Section 2.4) to calculate the lateral range in which heat dissipates in our specimen and the temperatures reached within that range. In **Figure 6**, the calculated temperature profile within the 50 μm-long bar of Au for the case of ns laser pulses with the selected fluence of 1.36 J cm^{-2} is overlaid on an SEM image of a corresponding P3 line edge. The region where the cross-sectional lamella shown in Figure 4 was cut, is also marked. Within the P3 line, the temperature decays quickly from its highest value of about 2800 K at the center of the line to about 400 K at the line edge. The STEM-EDX measurements (Figure 4) indicate a Br-rich phase within the first 12 μm from the left edge of the lamella; this corresponds to a region starting at a distance of about 25 μm from the scribe line center to a distance of about 37 μm. Within this region, the calculated temperature decays from about 400 K to $\approx$320 K. These results show that the lateral range where the Br-rich phase was observed is still exposed to elevated temperatures. This suggests that in addition to the known thermally induced decomposition of perovskite to PbI_2
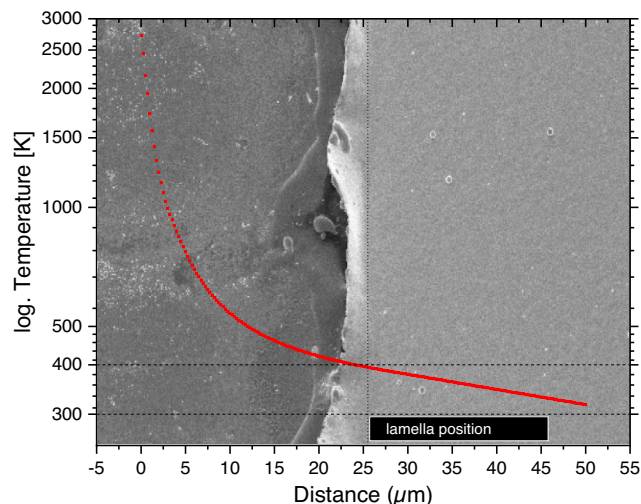
within the laser scribe line, an additional effect sets in: the formation of a Br-rich phase at the perovskite/HTL interface next to the P3 line edge; both are apparently induced by the spatial heat flow of the dissipated laser energy.

4. Conclusion

In this study, P3 patterning of PSMs by means of ns and ps pulsed laser was systematically investigated to reveal the influence of the laser pulse duration on the electrical behavior and chemical composition of PSMs. It is shown that both laser pulse durations can be successfully applied for P3 patterning, but the ns laser pulses result in better photovoltaic performance. Surface morphology imaging and compositional analysis of the P3 lines and its vicinity reveal that the application of ns laser pulses results in a larger amount of PbI_2 generated within the P3 lines compared with ps laser pulses. Moreover, ns laser pulses also induce the formation of a thin Br-rich layer at the perovskite/HTL interface for up to 12 μm from the P3 line edge, whereas the ps laser pulse does not. The calculation of the laser-induced surface temperature supports the conclusion that these compositional alterations were induced by the deposited thermal energy of the ns laser pulses. Both PbI_2 and the Br-rich layer improve the overall photovoltaic performance by passivating electronic defect states at the edges of the scribe line and blocking charge carriers in its vicinity. Based on this new understanding of laser-material interaction in P3 patterning, a PCE of more than 19% has recently been achieved for a three-cell PSM.[38]

Supporting Information

Supporting Information is available from the Wiley Online Library or from the author.

Acknowledgements

Conflict of Interest

The authors declare no conflict of interest.

Data Availability Statement

Research data are not shared.

Keywords

[1] J. S. Manser, J. A. Christians, P. V. Kamat, *Chem. Rev.* **2016**, *116*, 12956.

[2] S. Albrecht, M. Saliba, J. P. C. Baena, F. Lang, L. Kegelmann, M. Mews, L. Steier, A. Abate, J. Rappich, L. Korte, *Energy Environ. Sci.* **2016**, *9*, 81.

[3] T. Todorov, T. Gershon, O. Gunawan, Y. S. Lee, C. Sturdevant, L. Y. Chang, S. Guha, *Adv. Energy Mater.* **2015**, *5*, 1500799.

[4] E. L. Unger, L. Kegelmann, K. Suchan, D. Sorell, L. Korte, S. Albrecht, *J. Mater. Chem. A* **2017**, *5*, 11401.

[5] NREL, Champion Photovoltaic Module Efficiency Chart, in, NREL, NREL **2020**.

[6] B. Stegemann, C. Schultz, *Digital Encyclopedia Appl. Phys.* **2019**, https://doi.org/10.1002/3527600434.eap830.

[7] G. Mincuzzi, A. L. Palma, *ChemElectroChem* **2016**, *3*, 9.

[8] C. Schultz, M. Fenske, J. Dagar, A. Zeiser, A. Bartelt, R. Schlatmann, E. L. Unger, B. Stegemann, *Sol. Energy* **2020**, *198*, 410.

[9] C. Schultz, F. Schneider, A. Neubauer, A. Bartelt, M. Jošt, B. Rech, R. Schlatmann, S. Albrecht, B. Stegemann, *IEEE J. Photovoltaics* **2018**, *8*, 1244.

[10] F. Matteocci, L. Vesce, F. U. Kosasih, L. A. Castriotta, S. Cacovich, A. L. Palma, G. Divitini, C. Ducati, A. Di Carlo, *ACS Appl. Mater. Interfaces* **2019**, *11*, 25195.

[11] S.-J. Moon, J.-H. Yum, L. Löfgren, A. Walter, L. Sansonnens, M. Benkhaira, S. Nicolay, J. Bailat, C. Ballif, *IEEE J. Photovoltaics* **2015**, *5*, 1087.

[12] F. U. Kosasih, L. Rakocevic, T. Aernouts, J. Poortmans, C. Ducati, *ACS Appl. Mater. Interfaces* **2019**, *11*, 45646.

[13] S. Haas, A. Gordijn, H. Stiebig, *Prog. Photovoltaics: Res. Appl.* **2008**, *16*, 195.

[14] A. Merdasa, M. Bag, Y. Tian, E. Källman, A. Dobrovolsky, I. G. Scheblykin, *J. Phys. Chem. C* **2016**, *120*, 10711.

[15] B. Roose, K. Dey, Y.-H. Chiang, R. H. Friend, S. D. Stranks, *J. Phys. Chem. Lett.* **2020**, *11*, 6505.

[16] F. Liu, Q. Dong, M. K. Wong, A. B. Djurišić, A. Ng, Z. Ren, Q. Shen, C. Surya, W. K. Chan, J. Wang, *Adv. Energy Mater.* **2016**, *6*, 1502206.

[17] S. Shukla, S. Shukla, L. J. Haur, S. S. H. Dintakurti, G. Han, A. Priyadarshi, T. Baikie, S. G. Mhaisalkar, N. Mathews, *ChemSusChem* **2017**, *10*, 3804.

[18] T. Du, C. H. Burgess, J. Kim, J. Zhang, J. R. Durrant, M. A. McLachlan, *Sustainable Energy Fuels* **2017**, *1*, 119.

[19] L. Wang, C. McCleese, A. Kovalsky, Y. Zhao, C. Burda, *J. Am. Chem. Soc.* **2014**, *136*, 12205.

[20] J. Barbé, M. Newman, S. Lilliu, V. Kumar, H. K. H. Lee, C. Charbonneau, C. Rodenburg, D. Lidzey, W. C. Tsoi, *J. Mater. Chem. A* **2018**, *6*, 23010.

[21] J. Dagar, K. Hirselandt, A. Merdasa, A. Czudek, R. Munir, F. Zu, N. Koch, T. Dittrich, E. L. Unger, *Sol. RRL* **2019**, *3*, 1900088.

[22] E. H. Anaraki, A. Kermanpur, L. Steier, K. Domanski, T. Matsui, W. Tress, M. Saliba, A. Abate, M. Grätzel, A. Hagfeldt, J.-P. Correa-Baena, *Energy Environ. Sci.* **2016**, *9*, 3128.

[23] L. Kegelmann, C. M. Wolff, C. A. Omondi, F. Lang, E. L. Unger, L. Korte, T. Dittrich, D. Neher, B. Rech, S. Albrecht, *ACS Appl. Mater. Interfaces* **2017**, *9*, 17245.

[24] J. M. Liu, *Opt. Lett.* **1982**, *7*, 196.

[25] F. U. Kosasih, C. Ducati, *Nano Energy* **2018**, *47*, 243.

[26] F. U. Kosasih, S. Cacovich, G. Divitini, C. Ducati, *Small Methods* **2021**, *5*, 2000835.

[27] F. de la Peña, V. T. Fauske, P. Burdet, E. Prestat, P. Jokubauskas, M. Nord, T. Ostasevicius, K. E. MacArthur, M. Sarahan, D. N. Johnstone, J. Taillon, A. Eljarrat, V. Migunov, J. Caron, T. Furnival, S. Mazzucco, T. Aarholt, M. Walls, T. Slater, F. Winkler, B. Martineau, G. Donval, R. McLeod, E. R. Hoglund, I. Alxneit, I. Hjorth, T. Henninen, L. F. Zagonel, A. Garmannslund, A. Skorikov, *Hyperspy* **2018**, https://doi.org/10.5281/ZENODO.1469364.

[28] N. M. Bulgakova, A. V. Bulgakov, *Appl. Phys. A: Mater. Sci. Process.* **2001**, *73*, 199.

[29] A. V. Bulgakov, N. M. Bulgakova, *Quantum Electron.* **1999**, *29*, 433.

[30] N. M. Bulgakova, I. M. Bourakov, *Appl. Surf. Sci.* **2002**, *197–198*, 41.

[31] N. M. Bulgakova, A. V. Bulgakov, L. P. Babich, *Appl. Phys. A: Mater. Sci. Process.* **2004**, *79*, 1323.

[32] Y. P. Meshcheryakov, N. Bulgakova, *Appl. Phys. A: Mater. Sci. Process.* **2006**, *82*, 363.

[33] B.-W. Park, N. Kedem, M. Kulbak, D. Y. Lee, W. S. Yang, N. J. Jeon, J. Seo, G. Kim, K. J. Kim, T. J. Shin, G. Hodes, D. Cahen, S. I. Seok, *Nat. Commun.* **2018**, *9*, 3301.

[34] E. J. Juarez-Perez, L. K. Ono, M. Maeda, Y. Jiang, Z. Hawash, Y. Qi, *J. Mater. Chem. A* **2018**, *6*, 9604.

[35] K. T. Cho, S. Paek, G. Grancini, C. Roldán-Carmona, P. Gao, Y. Lee, M. K. Nazeeruddin, *Energy Environ. Sci.* **2017**, *10*, 621.

[36] R. Ahuja, H. Arwin, A. Ferreira da Silva, C. Persson, J. Osorio-Guillén, J. Souza de Almeida, C. Moyses Araujo, E. Veje, N. Veissid, C. An, *J. Appl. Phys.* **2002**, *92*, 7219.

[37] S. M. Jain, B. Philippe, E. M. J. Johansson, B.-W. Park, H. Rensmo, T. Edvinsson, G. Boschloo, *J. Mater. Chem. A* **2016**, *4*, 2630.

[38] J. Dagar, M. Fenske, A. Al-Ashouri, C. Schultz, B. Li, H. Köbler, R. Munir, G. Parmasivan, J. Li, L. Levine, A. Merdasa, D. Többens, T. Dittrich, R. Schlatmann, B. Stegemann, A. Abate, S. Albrecht, E. Unger, Compositional and Interfacial Engineering Yield High-Performance and Stable P-I-N Perovskite Solar Cells and Mini-Modules, Unpublished **2020**.

[39] S. Wolfram, Au Wolfram Alpha Computational Intelligence, www.wolframalpha.com (accessed: December 2020).

[40] P. B. Johnson, R. W. Christy, *Phys. Rev. B* **1972**, *6*, 4370.